Chemosphere 212 (2018) 79–86

Contents lists available at ScienceDirect

Chemosphere

journal homepage: www.elsevier.com/locate/chemosphere

Photoelectrocatalytic reduction of nitrobenzene on Bi-doped $CuGaS_2$ films

Marcos A.S. Andrade Jr., Lucia H. Mascaro*

Department of Chemistry, Federal University of São Carlos, Rod. Washington Luiz, Km 235, CEP 13565-905 São Carlos, SP, Brazil

HIGHLIGHTS

- Facile and fast approach to prepare Bismuth-doped $CuGaS_2$ nanocrystals.
- Bismuth-doping enhanced optical properties of the chalcogenide semiconductor.
- Photoelectrocatalytic reduction of nitrobenzene under visible light irradiation.
- High conversion and high selectivity to aniline using Bi-doped $CuGaS_2$.

GRAPHICAL ABSTRACT

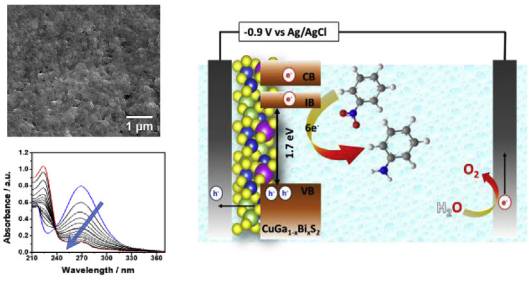

ARTICLE INFO

Article history:
Received 7 May 2018
Received in revised form
13 August 2018
Accepted 14 August 2018
Available online 15 August 2018

Handling Editor: E. Brillas

Keywords:
Photoelectrocatalysis
Nitrobenzene
Chalcogenide
Bismuth

ABSTRACT

Nitrobenzene, a toxic nitroaromatic, a feedstock compound to the production of many commercially relevant chemicals were photoelectrocatalytically reduced into aniline on a photoelectrode comprised by a bismuth-doped $CuGaS_2$ nanocrystallyne thin films on molybdenum. The activity of the photoelectrodes were compared to the reaction performed on undoped-$CuGaS_2$ films, and they were carried out under illumination with an applied bias potential at 0.9 V. Aniline was highly selectively obtained with 83% of conversion for reaction times of 100 min when using Bi-doped $CuGaS_2$, representing higher conversion of nitrobenzene and yield to aniline than the undoped photoelectrode. The catalytic performance of the doped films remained stable for a set of 5 consecutive experiments. These results indicate Bi-doped $CuGaS_2$ as a promising material to be applied in the photoelectrocatalytic reduction of nitrobenzene into aniline through the direct pathway mechanism, using solar light illumination.

1. Introduction

Nitrobenzene (NB) derivatives are a class of compounds that find high applicability in the production of many commercially relevant chemicals, such as dyes (Rao et al., 2003), explosives (Tan et al., 2017), pesticides (Keum and Li, 2004) and perfumes (Ma et al., 2017), to name a few. In the pharmaceutical industry, NB derivatives can be used as precursors in different synthesis routes (Roberts et al., 2017) such as in the paracetamol synthesis (Khan et al., 2017; Marsac et al., 2017) for instance. A major cause of concern due to the large use of nitroaromatics by the industry is the persistent presence of such pollutants in wastewater effluents and the toxicological implications to the human health (Zhu et al., 2007). NB have already been linked to anemia, skin irritation and presumably have carcinogenic nature (Kovacic and Somanathan, 2014; Li et al., 2017a). According to United States Environment Protection Agency (USEPA), its maximum allowed concentration in wastewater must not exceed 20 ppb (Lowenbach et al., 1979; Liu et al., 2017a; b). Over the past decades, many research groups

* Corresponding author.
E-mail addresses: marcos_asaj@hotmail.com (M.A.S. Andrade), lmascaro@ufscar.br (L.H. Mascaro).

https://doi.org/10.1016/j.chemosphere.2018.08.071
0045-6535/

have reported different strategies to manage nitroaromatics in aqueous effluents, such as physical (Wu et al., 2017), biological (Li et al., 2017b; Yuan et al., 2017), and chemical degradation techniques (Bai et al., 2017; Yang et al., 2018). It is commonly pointed as an effective and environmentally friendly strategy to convert the toxic nitrobenzene into a low toxic and easy to mineralize amino-aromatic derivative (Liu et al., 2017a; b). In this sense, several investigations have reported the usage of noble metals (Au, Pt) and transition metals (Ru, Cu, Ni) in the production of aniline and intermediates (nitrosobenzene, phenylhydroxylamine, azobenzene) from the heterogeneous catalytic hydrogenation of nitrobenzene (Sheng et al., 2016). However, some of these methods require the employment of elevated temperatures and H_2 pressure conditions in order to obtain satisfactory yields of aniline (Qusti et al., 2014). As an alternative, electrochemical reduction of nitrobenzene to aniline over noble metal electrodes (Pt, Au) has also been reported. The main drawback of the electrocatalytic approach is the low current efficiencies obtained since nitrobenzene reduction takes place at considerably highly negative values of overpotential, in such a way that the undesired hydrogen reduction reaction also occurs concomitantly (Marken et al., 1996; Seshadri and Kelber, 1999). To overcome this issue, many studies have focused in the development of cathodic materials able to promote the nitrobenzene reduction at lower overpotentials (Song et al., 2007).

On the other hand, photocatalysis has attracted much attention since TiO_2 electrodes began to be employed in the light-assisted decomposition of water into hydrogen and oxygen (Fujishima and Honda, 1972). It expanded the investigations on using photochemical catalysis, not only for water splitting (Kanakaraju et al., 2015; Gao et al., 2017a; b; Gromboni et al., 2017), but also for organic pollutants degradation (Alves et al., 2018), carbon dioxide reduction to fuels (Gao et al., 2017a; b), among other organic reactions (Wang et al., 2017). This technique provides prominent advantages including non-toxicity, low cost, no secondary pollution and thorough mineralization. In addition, photocatalysis can be performed under solar illumination as a renewable and alternative energy resource.

The photoelectrocatalysis combines electrocatalysis and photocatalysis, where a system containing a photoelectrode is activated by light illumination with an application of a constant bias potential. In this system, the photocatalyst can be easily recovered and recycled for consecutives treatments after use (Xie et al., 2016; Garcia-Segura and Brillas, 2017).

The photoelectrocatalytic efficiency on organic pollutant remediation is directly related to the semiconductor selected as photoelectrodes. In this work, a thin filme of $CuGaS_2$ on molybdenum is used as photoelectrode. $CuGaS_2$ is a chalcogenide (Cu-III-S_2 family) (Tablero and Marron, 2010) with a 2.4 eV band gap (E_g) (M. Han et al., 2016a, b) of chalcopyrite-like structure (Song et al., 2015; Guo et al., 2016). Its optical absorption can be enhanced to produce photocatalysts that are active in the visible light range when doped with transition metals (Ti (Hashemi et al., 2014; Jing et al., 2016; Lv et al., 2014), Cr (Chen et al., 2013), Ce (Xiao et al., 2015) and Fe (Koskelo et al., 2016)), post-transition (Sn (Song et al., 2015; Han et al., 2016a; b)), and 15 group elements (N, P, As, Sb) (Han et al., 2016a; b). Han et al. (Han et al., 2016a; b). Inspired by the aforementioned strategy herein we present the development of a Bi-doped $CuGaS_2$ nanocrystals and its catalytic performance evaluation towards the selective reduction of nitrobenzene into aniline, using a photoelectrocatalytic approach.

2. Experimental

2.1. Chemicals

In this work the following chemicals were used: copper (I) chloride (CuCl, 97%, Sigma Aldrich), gallium sulfate ($Ga_2(SO_4)_3 \cdot 18H_2O$, 99.99%, Aldrich), sulfur powder (S, 99.5%, Acros), bismuth nitrate ($Bi(NO_3)_3 \cdot 5H_2O$, 98%, Sigma Aldrich), oleylamine (OLA) (70%, Sigma Aldrich), molybdenum foil (Mo 0.1 mm, Sigma Aldrich), nitrobenzene (NB) (99.98%, Vetec Quimica Fina).

2.2. Synthesis of Bi-doped $CuGaS_2$ chalcopyrite nanocrystals

Bi-doped $CuGaS_2$ nanocrystals were prepared according to the procedure reported in our previous work (Andrade and Mascaro, 2018). In the procedure, 0.5 mmol of CuCl, 0.24 mmol of $Ga_2(SO_4)_3 \cdot 18H_2O$, and 0.01 mmol of $Bi(NO_3)_3 \cdot 5H_2O$ were added to 8 mL of OLA into a three-neck flask. In a separate flask, 1 mmol of sulfur powder was dissolved in OLA (2 mL). Both flasks were attached to a Schlenk line, previously purged of oxygen and water by pulling vacuum at room temperature for 10 min. The flasks were heated to 240 °C using a sand bath, and then, the reaction was initiated by the rapid transfer of the sulfur precursor into the metals solution. The reaction mixture was refluxed for 1 h and allowed to cool to room temperature. The nanocrystals were separated by precipitation, adding excess ethanol followed by centrifugation at 8000 rpm for 10 min. Thereafter, the nanocrystals were redispersed in chloroform and centrifuged at 7000 rpm for 5 min. To remove excess OLA, the product was again precipitated with ethanol, centrifuged and finally, stored in hexane.

2.3. Spray-deposition of nanocrystals on Mo substrates

For depositing Bi-doped $CuGaS_2$ films on a Mo foil, a spray system was assembled using an airbrush tool attached to a compressed air line (10 mL min^{-1}), used as solution carrier (Fig. SM-1). The nanocrystals hexane solutions (0.012 mg mL^{-1}) were sprayed for 2 s (spray flow = 33 μL s^{-1}) on preheated Mo substrates (5 mm × 10 mm) on a hotplate at 80 °C. This process was then repeated 20 times, with 1 min intervals between the deposition sessions for evaporation of the remaining solvent.

2.4. Bi-doped $CuGaS_2$ nanocrystals and nanocrystalline films characterization

The organization at long-distance and structure of the chalcogenides were determined by X-ray powder diffraction (XRD) analysis, performed with Cu Kα radiation (40 kV, 30 mA) using a Shimadzu model XRD 6000 diffractometer with 0.5°, 0.5°, 0.3 mm slits for entrance, scattering and exit, respectively, at room temperature. The UV–Vis spectra of the nanocrystals solutions were measured between 300 and 2000 nm in a quartz cell with a 1 cm path length, using a Cary 5G Varian UV–Vis–NIR spectrophotometer. Transmition electron microscopy (TEM) and high-resolution (HRTEM) images were obtained using a Tecnai G2 F20 X-Twin 200 kV FEI. Films thicknesses and semiquantitative elemental analysis were estimated by scanning electron microscopy (SEM, Inspect F50 model, FEI) coupled with energy dispersive X-ray spectroscopy (EDS). X-ray photoelectron spectroscopy (XPS) measurements were performed on a Thermo Scientific K-Alpha spectrometer using monochromatic Al Kα (1486.6 eV) radiation.

2.5. Photoelectrocatalytic reduction of nitrobenzene on $CuGa_{1-x}Bi_xS_2$ films

Photoelectrocatalytic experiments were carried out in a quartz cell equipped with an Ag/AgCl reference electrode, a Pt counter electrode, and $CuGa_{1-x}Bi_xS_2$ films supported on Mo with a 0.25 cm^2 average active area, as working electrode. The electrodes were immersed in 3.5 mL electrolyte solution, containing 80 μM

nitrobenzene, phosphate buffer (0.1 M, pH = 7.0) and Na_2SO_4 (0.5 M), under N_2 bubbling. During NB photoelectroreduction experiments, the working electrode was illuminated by a 100 mW cm^{-2} Xenon lamp (AM 1.0G) and concomitantly, an overpotential of −0.9 V (versus Ag/AgCl/saturated KCl) was applied. The reactant consumption and the resulting products were analyzed by an UV–Vis–NIR Cary 5G Varian spectrophotometer and by a Shimadizu GC-MS. Purely photocatalytic and electrocatalytic experiments were also performed as control essays in order to compare the methods. All batch experiments were performed in triplicate. Overall conversions of NB, yield and selectivity of aniline were calculated according to the equations (Zhang et al., 2017):

$$\text{Conversion}\ (\%) = \left[\frac{(C_0 - C_{NB})}{C_0}\right] \times 100 \quad (1)$$

$$\text{Yield}\ (\%) = \frac{C_{AN}}{C_0} \times 100 \quad (2)$$

$$\text{Selectivity}\ (\%) = \left[\frac{C_{AN}}{(C_0 - C_{NB})}\right] \times 100 \quad (3)$$

Where C_0 is the initial concentration of NB, C_{NB} is the final concentration of NB after reaction, and C_{AN} the final concentration of aniline after reaction.

The Faradaic efficiencies (η) for the electrochemical and photoelectrochemical reactions were calculated according to the equation:

$$\eta = \frac{nFC_{AN}v}{Q} \quad (4)$$

Where n is the number of moles electrons required to reduce nitrobenzene into nailine, F is the Faraday constant, v is the volume, and Q is the measured charge (Chen et al., 2015). The η was not calculated for photocatalytic reactions, once no potential was applied, consequently, the charge was not measured.

3. Results and discussion

3.1. Characterization of Bi-doped $CuGaS_2$ films

The XRD diffractograms (Fig. 1a–b) of the ternary chalcogenides, $CuGaS_2$ and Bi-doped $CuGaS_2$ nanocrystals with 15 nm average particle size (Fig. SM-2) show the main peaks (112), (220)/(204), and (312) centered around 29, 48, and 57° 2θ (Chang et al., 2014), -respectively, well indexed with the chalcopyrite $CuGaS_2$ (JCPDS: 75–0103), with the characteristic tetragonal cell with space group $I\bar{4}2d$ (Fig. 1-c) (Han et al., 2016a; b). High purity photocatalyst were obtained since there are no peaks related to $CuBi_xS_y$, Cu_xS or Ga_xS phases in the diffractograms. The (112) and (220)/(204) peaks in Bi-doped $CuGaS_2$ diffractogram (Fig. 1b) shift approximately 1° to lower 2θ degree in comparison to the observed for $CuGaS_2$ samples. This shift corresponds to a 0.3 Å interplanar distance increment and may be associated with the fact that Bi atomic *radius* (1.48 Å) is larger than that of Ga (1.22 Å) (Cordero et al., 2008). Once some Bi^{3+} are placing at Ga^{3+} position in the doped chalcopyrite nanocrystals, Bi–S bond length is larger than that in the Ga–S bond (2.32 Å) (Han

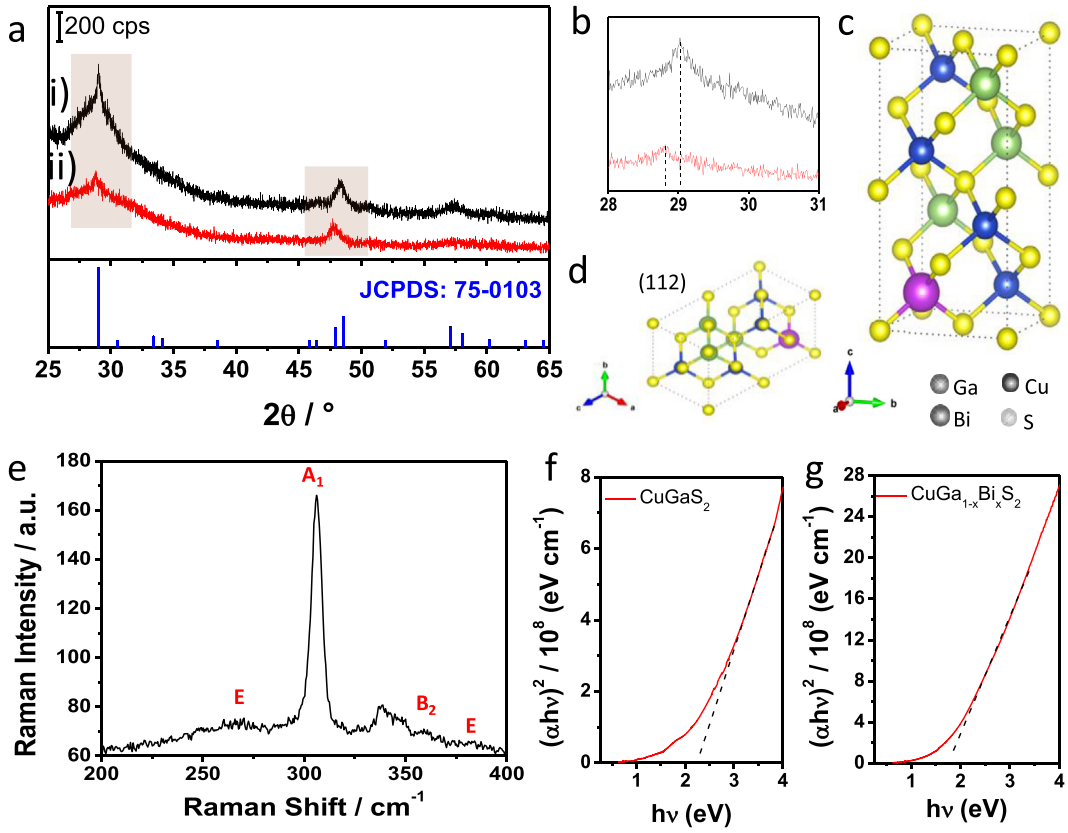

Fig. 1. a) XRD diffractograms of i) $CuGaS_2$ and ii) $CuGa_{1-x}Bi_xS_2$. b) Zoomed region of the XRD diffractogram showing the (112) peak shift to lower 2θ degree in the doped sample. c) Graphic representation of the crystal structure of Bi-doped $CuGaS_2$. d) Graphic representation of the (112) plane in the crystal structure of Bi-doped $CuGaS_2$. e) Raman spectrum of $CuGa_{1-x}BixS_2$. f) and g) show the Tauc plots for $CuGaS_2$ and $CuGa_{1-x}Bi_xS_2$ nanocrystals in hexane, respectively.

et al., 2016a; b), increasing spacing distances of the (112) and (220)/(204) planes in up to 2 p.m. (Fig. 1d).

Raman spectroscopy is very useful to characterize chalcopyrites. The more intense band at 305 cm^{-1} (Fig. 1e) correspond to the A_1 optical vibration mode which is the dominant active mode in chalcopyrite, assigned to vibrations of sulfur atoms, while the others are stationary (Cao et al., 2017). In pure $CuGaS_2$ this vibration is located around 310 cm^{-1} and the shift to lower frequencies in the Bi-doped ternary sulfide is attributed to mass and electronegativity differences (Chen et al., 2013). The B_2 and E modes assigned at 364 and 386 cm^{-1}, respectively, correspond to the vibrations of Ga–S bond, and the E mode at 274 cm^{-1}, to the vibration of Cu–S (Cao et al., 2017). The new appearing band at 338 cm^{-1} may be related to the incorporation of Bi into the structure. The good agreement of the results presented here with previous reported in literature (Cao et al., 2017) further confirm the obtaining of pure Bi-doped chalcopyrite nanocrystals.

Optical properties of CuGaS and Bi-doped $CuGaS_2$ nanocrystals were analyzed using UV–Vis–NIR spectroscopy. The direct band gap values of the chalcogenides were estimated at 2.3 eV in the $CuGaS_2$ and 1.7 eV in the $CuGa_{1-x}Bi_xS_2$ (dashed red lines in Fig. 1f–g) by extrapolating the $(\alpha h\nu)^2$ *vs* energy photon profile on the Tauc plots. The optical band gap of the $CuGaS_2$ nanocrystals prepared here coincides well with that reported in the literature for typical tetragonal chalcopyrites, which is between 2.3 and 2.5 eV (Kim et al., 2008; Subbaramaiah and Raja, 1992; Ullah et al., 2018). The E_g of $CuGa_{1-x}Bi_xS_2$ decreased with Bi incorporation, resulting in absorption at a higher range of the visible light spectrum, what increases the photon harvesting properties (Ullah et al., 2018). Similar results have been reported by Ti (Palacios et al., 2008), V (Strandberg and Aguilera, 2012), Cr (Ahsan et al., 2017), Ni (Han et al., 2014) and Fe (Aksenov et al., 1992) doping in chalcogenides. According to some authors, the incorporation of metals in $CuGaS_2$ would generate an intermediate band which can enhance the absorption of low energy photons, allowing the promotion of electrons from the valence band to the conduction band using two photons with energies below the band gap (Han et al., 2014; Han et al., 2016a; b; Wang et al., 2016).

The films average thicknesses (Fig. 2) are estimated to be around 2.3–2.5 μm (Fig. 2a–b). The $CuGaS_2$ and $CuGa_{1-x}Bi_xS_2$ films show an irregular structure formed by the aggregation of *quasi*-spherical nanocrystals. The stoichiometry of the films was calculated based on a semiquantitative elemental analysis by EDS. Based on the obtained data, the $CuGaS_2$ film presents a Cu:Ga:S percentual atomic ratio equal to 1:1.02:2.13 and Bi-doped $CuGaS_2$ samples present a Cu:Ga:Bi:S ratio equal to 1:0.97:0.01:2.17, suggesting the Bi-doped stoichiometry to be $CuGa_{0.97}Bi_{0.01}S_{2.17}$.

3.2. Nitrobenzene reduction over $CuGa_{1-x}Bi_xS_2$ films

Nitrobenzene reduction process can generate several compounds depending on experimental conditions such as applied potential, pH, and catalyst used (Li et al., 2007). The different products from nitrobenzene reduction include phenylhydroxylamine, nitrosobenzene, aniline, azoxybenzene, and azobenzene, for instance (Wang et al., 2011; Mondal and Purkait, 2017). Among these products, aniline exhibits the lowest toxicity and the best biodegradability (Li et al., 2017a; b; c) and it is therefore, a highly desirable product from the treatment of wastewater containing nitrobenzene. In this sense, the performance of the $CuGaS_2$ and Bi-doped $CuGaS_2$ films were evaluated towards the selectivity of nitrobenzene reduction to aniline.

Initially, cyclic voltammetry measurements were performed in both dark and illumination conditions, as depicted in Fig. 3a (Electrolyte composition: 80 μM nitrobenzene + 0.5 M Na_2SO_4 + 0.1 M phosphate buffer pH 7.0). The voltammograms show an anodic peak associated to the nitrobenzene reduction to aniline at −0.76 V (*vs*. Ag/AgCl). The reduction potential observed here is close to that reported by Challagula et al. (Challagulla et al., 2017) for the nitrobenzene reduction to aniline over TiO_2 and graphitic carbon electrodes in 0.1 M Na_2SO_4 electrolyte. The black curve represents the reduction process of nitrobenzene into aniline in the dark in a mechanism involving the transfer of 6 electrons (Seshadri and Kelber, 1999). Under illumination, the reduction currents slightly increased (Fig. 4 - red curve), indicating some activity of the electrodes under the presence of visible light, in addition, it is observed a positive shift (~25 mV) at the onset potential, which is a typical behavior in photocatalysts.

The semiconductor film is expected to be activated by light irradiation, due to the promotion of electrons from the valence band to the conduction band, increasing the reducing properties of the electrode (Fig. 3b). On the other hand, the photo-generated

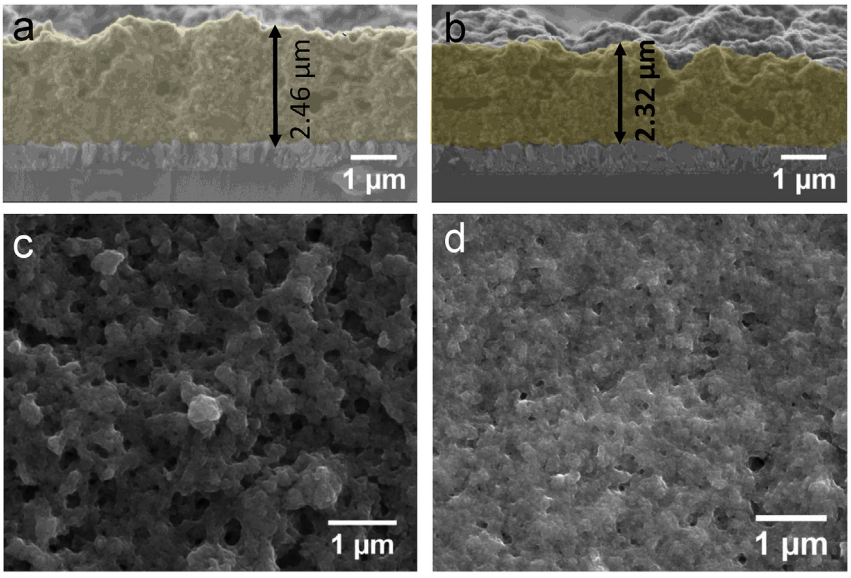

Fig. 2. Cross-sectional and top view SEM micrographs of $CuGaS_2$ and $CuGa_{1-x}Bi_xS_2$ films.

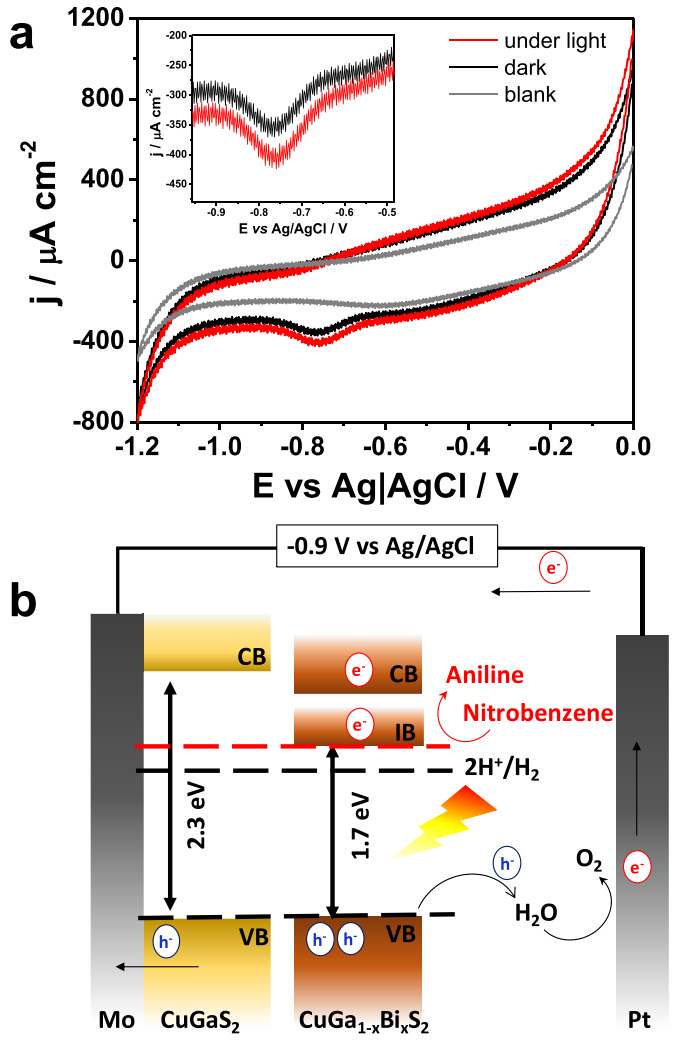

Fig. 3. a) Typical cyclic voltammograms at 50 mV s^{-1} for $CuGa_{1-x}Bi_xS_2$/Mo electrodes in the presence of nitrobenzene, at pH 7.0, in the dark (black curve) and under 100 W cm^{-2} illumination (red curve). The gray curve represents the blank, in absence of nitrobenzene. Inset: Zoomed region of the voltammograms showing the reduction peak. b) p-type semiconductors relative to the water redox potentials and reduction potential of the nitrobenzene into aniline, suggesting that the narrower band gap in $CuGa_{1-x}Bi_xS_2$ favors nitrobenzene reduction. (For interpretation of the references to colour in this figure legend, the reader is referred to the Web version of this article.)

holes promote water oxidation, as reported by Su et al. in the photocatalytic solar water splitting systems using chalcogenides with the maximum energy of the valence band lower than the water oxidation potential, for example, the systems $CdIn_2S_4$, Cu_2ZnSnS_4, and $CuBaSnS_4$ (Ali et al., 2017; Su et al., 2017).

Once determined the nitrobenzene potential reduction into aniline, the photoelectrocatalytic experiments were carried out applying constant potential at −0.9 V (versus Ag|AgCl| saturated KCl) to guarantee that, in this potential, all the nitrobenzene was converted into aniline.

The photoelectrocatalytic performance of the $CuGaS_2$-based films was examined under visible light irradiation (100 W cm^{-2}), in oxygen-free atmosphere. In addition, the performance of $CuGa_{1-x}Bi_xS_2$ is presented in comparison with that observed on $CuGaS_2$-deposited on Mo electrodes, under different experimental conditions: only under illumination (photocatalysis) and under applied potential solely (electrocatalysis).

The real-time monitoring nitrobenzene reduction by UV–Vis spectroscopy was evaluated by the peak centered at 270 nm, assigned to nitrobenzene, decreases with time meanwhile the peak at 230 nm, attributed to aniline, increases, as the major product of the reaction (Fig. SM-4).

Fig. 4a–b shows the electrochemical reduction of nitrobenzene into aniline on $CuGaS_2$ and Bi-doped $CuGaS_2$ films deposited on molybdenum electrodes. As one observes, around 56% (Table 1) of nitrobenzene has been reduced to aniline when using $CuGaS_2$ electrodes by applying a potential of −0.9 V, in dark conditions. The electrocatalytic reduction of nitrobenzene improves when using Bi-doped $CuGaS_2$ electrodes (nitrobenzene reduction ~75%, Fig. 4b). However, the curve shows that the final concentration of aniline (27.3 ± 0.7 μM) is rather lower than the initial concentration of nitrobenzene (76.3 ± 0.2 μM), which means that the yield and the selectivity of this reaction to aniline are quite low (~35%, and ~46%, respectively, Table 1). Although no peaks other than aniline or nitrobenzene were observed in the chromatograms, it suggests the aniline produced during the electrochemical reduction of nitrobenzene may result in polymerization on the electrode surface.

In all photocatalytic reduction experiments (Fig. 4c–d), using both catalysts films, the reactant was selectively reduced to aniline after 100 min, under visible light irradiation, presenting yields higher than 70%. Bi-doped chalcogenide film presented a high conversion of nitrobenzene into aniline (~83%), which corresponds to an average conversion enhancement of 20% in comparison to the same process over the undoped film.

Photoelectrocatalytic reduction using $CuGaS_2$ electrodes (Fig. 4e) converted around 70% of nitrobenzene within 100 min of reaction under illumination conditions. In the case of $CuGa_{1-x}Bi_xS_2$ electrodes, nitrobenzene reduction is significantly increased up to 83% in average, totally selective to aniline presenting the highest yield (approximately 84%) in comparison to the other approaches performed in this work, indicating that the proposed band gap decrement due to the Bi-doping indeed contributes to the photocatalytic activity improvement. Although the systems using $CuGa_{1-x}Bi_xS_2$/Mo photoelectrodes (Fig. 4f) presented higher conversions than the system using the undoped material, the combination of electro and photochemical approach do not clearly show significant synergistic effect. The conversion of nitrobenzene by photocatalysis or photoelectrocatalysis is quite similar. However, the photoelectrochemical approach provides high yield of a totally selective production of aniline. In addition, the faradaic efficiency for the conversion into aniline by photoelectrocatalysis on $CuGa_{1-x}Bi_xS_2$ electrodes is higher than that to the electrocatalytic reaction, indicating an increased selectivity to produce aniline in competition with the side-reactions, for example, the hydrogen evolution.

Comparing the capacities of the photocathodes to reduce nitrobenzene normalized by their geometric area (Fig. 5a), it was observed that $CuGa_{1-x}Bi_xS_2$/Mo can convert approximately 40% more than $CuGaS_2$/Mo. The kinetic parameters were obtained by fitting the data to a pseudo-first order process (Table 2) (Lin and Wang, 2009; Liu et al., 2017a, b). Although the linear fitting model agrees very well with the data ($R^2 > 0.989$), no distinct increase in the pseudo first-order rate constant (k_{obs}) can be observed. The narrower bang gap in Bi-doping $CuGaS_2$ is the main reason for the higher catalytic conversion as commented elsewhere. However, the apparent rate constant does not increase in the same fashion as the conversion rates, when comparing both systems. Indeed, there are many aspects to ponder in rationalizing resulting k_{obs} of a photoelectrocatalytic process such as adsorption kinetics; proton generation; electron-hole generation and their recombination (Basha et al., 2010), for example.

In addition, recycling experiments were carried out to check the stability and reusability of the photoelectrodes. The electrodes were washed several times with water and ethanol before each reaction, and they were reused for subsequent five runs under the

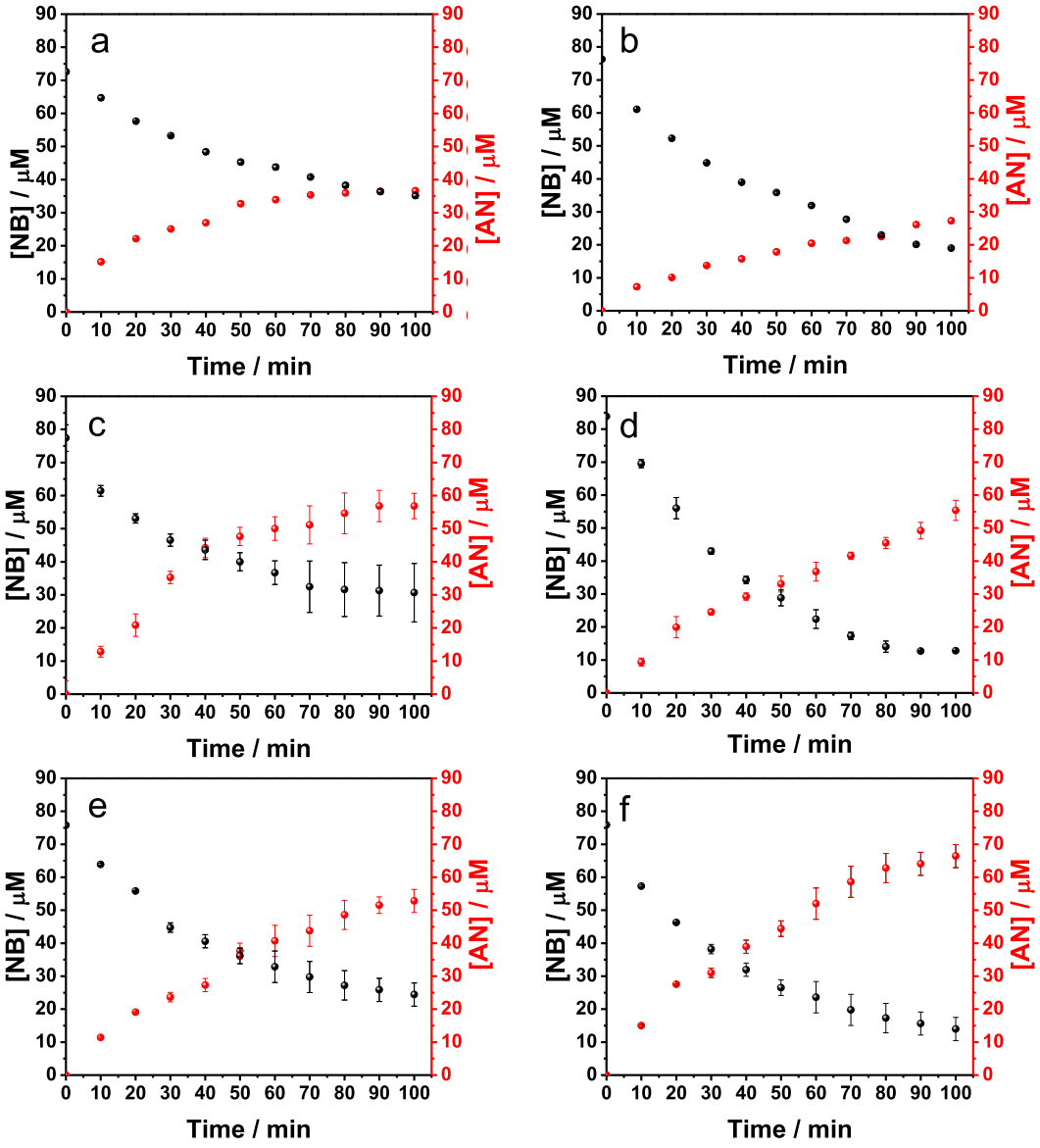

Fig. 4. Curves of (a, b) - electrocatalytic, (c, d) – photocatalytic, and (e, f) - photoeletrocatalytic reduction of nitrobenzene into aniline on films of $CuGaS_2$ (a, c, and e) and Bi-doped $CuGaS_2$ (b, d, and f).

Table 1
Average values of conversion of nitrobenzene, yield of aniline, and selectivity to aniline to the electro, photo, and photoelectrocatalytic reactions on $CuGaS_2$/Mo and $CuGa_{1-x}Bi_xS_2$/Mo photoelectrodes.

Method	**$CuGaS_2$/Mo**				**$CuGa_{1-x}Bi_xS_2$/Mo**			
	Conversion (%)	Yield (%)	Selectivity (%)	η (%)	Conversion (%)	Yield (%)	Selectivity (%)	η (%)
Electro	56 ± 1	47 ± 2	82 ± 2	15.7 ± 0.2	75 ± 1	35 ± 1	46 ± 1	15.3 ± 0.3
Photo	63 ± 7	70 ± 5	70 ± 12	–	83 ± 1	70 ± 5	91 ± 9	–
Photoelectro	70 ± 3	67 ± 4	95 ± 2	12.0 ± 0.4	83 ± 4	84 ± 3	98 ± 1	19.6 ± 0.5

following described experimental conditions: illumination of 100 mW cm^{-2}, applied potential of −0,9 V (vs Ag/AgCl/KCl), and reaction total time of 100 min. As shown in Fig. 5b, the photoelectrocatalytic activity of the $CuGaS_2$ films decreased in almost 20% after the third reaction. However, the catalytic activity of the $CuGa_{1-x}Bi_xS_2$ photoelectrodes remains approximately the same for the sequential five experiments without any significant change in the final conversion of nitrobenzene into aniline.

In terms of mechanism, the reduction of nitrobenzene into aniline using $CuGa_{1-x}Bi_xS_2$/Mo photoelectrode (Fig. SM-6) proceed involving six electrons. Herein, the reactions were carried out in an oxygen-free atmosphere thus, nitrobenzene is unlikely to undergo oxidation reactions. Moreover, when H_2O oxidizes, oxygen gas is released from the solution. Subsequently, the protons from water reduction and the photogenerated electrons react with nitrobenzene producing aniline. This can be safely assumed to take place in

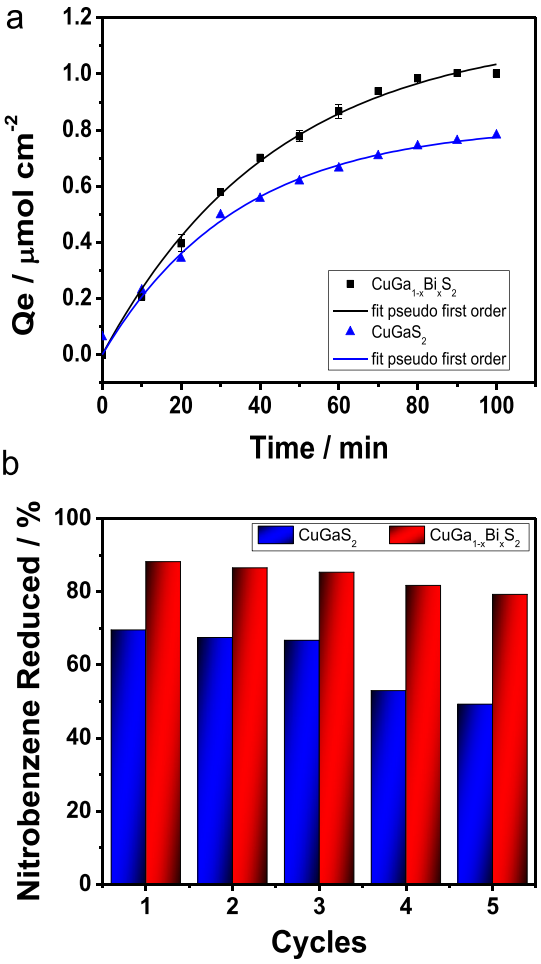

Fig. 5. a) Curves of capacity of nitrobenzene conversion normalized by the geometric area of the films. b) Cycling runs in photoelectroreduction of nitrobenzene into aniline at −0.9 V (vs Ag/AgCl/KCl) under visible light illumination of 100 mW cm^{-2} during 100 min.

Table 2
Pseudo-first order kinetic parameters of photoelectrocatalytic reduction of nitrobenzene on $CuGaS_2$ and $CuGa_{1-x}Bi_xS_2$/Mo films.

Photoelectrode	k_{obs}/min^{-1}	$Q_e/\mu mol\ cm^{-2}$	$\chi^2/10^{-16}$	R^2
$CuGaS_2$/Mo	0.029 ± 0.002	0.82 ± 0.02	6.22	0.989
$CuGa_{1-x}Bi_xS_2$/Mo	0.022 ± 0.001	1.15 ± 0.03	3.93	0.997

our experimental conditions once analyzing the products by GC-MS, no intermediates were identified (Fig. SM-6).

It is important to stress out that our results indicate that the phototoelectrochemical reduction of nitrobenzene into aniline on $CuGa_{1-x}Bi_xS_2$/Mo photocathode yields significant higher conversion than in many photocatalytic systems reported in literature using ternary chalcogenide or oxides catalysts, for instance: photocatalytic reduction of nitrobenzene on $CdIn_2S_4$ in benzyl alcohol solution (74% - during 6 h of illumination 300 W Xenon lamp (Ling et al., 2016)); photocatalytic reduction on Cd quantum dots (75% with time reaction of 55 h (Jensen et al., 2016)); and photocatalytic reduction on Ce-doped UiO-66/graphene nanocomposites (80% under 6 h under illumination 500 W Xe Lamp λ. 400 nm (Yang et al., 2017)). These comparisons show that Bi-doped $CuGaS_2$ is a promising material to be applied in the photoelectrocatalytic reduction of nitrobenzene, and more importantly, selectively producing aniline with high yields in a quite short reaction time.

4. Conclusions

In this study, Bi-doped $CuGaS_2$ and $CuGaS_2$ nanocrystalline films on molybdenum were applied to reduce nitrobenzene in aqueous solution by electro, photo, and photoelectrocatalytic approaches. The incorporation of bismuth into the $CuGaS_2$ chalcopyrite structure favored the reduction of nitrobenzene, because of the decreased band gap and broader spectral response, improving the light absorption within the visible-range in comparison to the undoped chalcopyrite. Using this photoelectrode, 83% of nitrobenzene were photoelectrochemically converted into aniline, and this compound was produced with high yield and high selectivity. Moreover, the electrodes stability and reusability were guaranteed for five sequential reactions, without any significant conversion losses. Therefore, nanocrystalline bismuth-doped $CuGaS_2$/Mo films function as an efficient photocathode to easily reduce nitrobenzene to aniline in aqueous environment in reasonably shorter times than equivalent systems reported in the literature. Its broad absorption in the visible range of light spectrum may encourage the nitrobenzene reduction from wastewater under solar light illumination.

Acknowledgments

The authors acknowledge Fundação de Amparo à Pesquisa no Estado de São Paulo, FAPESP (grant #2017/15144-9), FAPESP/GSK (grant #2014/50249-8), FAPESP/CDMF (grant #2013/07296-2) and Coordenação de Aperfeiçoamento de Pessoal de Nível Superior, CAPES (PNPD grant) for the financial support to this work.

Appendix A. Supplementary data

Supplementary data related to this article can be found at https://doi.org/10.1016/j.chemosphere.2018.08.071.

References

Ahsan, T., Kalainathan, S., Miyashita, N., Hoshii, T., Okada, Y., 2017. Characterization of Cr doped $CuGaS_2$ thin films synthesized by chemical spray pyrolysis. Mech. Mater. Sci. Eng. MMSE J. 9, 380–387.
Aksenov, I., Kudo, Y., Sato, K., 1992. Optical absorption spectra in $CuAlS_2$ doped with vanadium. Jpn. J. Appl. Phys. 1359, L145–L147.
Ali, A., Li, X., Song, J., Yang, S., Zhang, W., Zhang, Z., Xia, R., Zhu, L., Xu, X., 2017. Nature-mimic ZnO nanoflowers architecture: chalcogenide quantum dots coupling with $ZnO/ZnTiO_3$ nanoheterostructures for efficient photoelectrochemical water splitting. J. Phys. Chem. C 121, 21096–21104.
Alves, S.A., Goulart, L.A., Mascaro, L.H., 2018. A novel WO_3/MoS_2 photocatalyst applied to the decolorization of the textile dye Reactive Blue 198. J. Solid State Electrochem. 22, 1449–1458.
Andrade, M.A.S., Mascaro, L.H., 2018. Bismuth doping on $CuGaS_2$ thin films: structural and optical properties. MRS Commun. 1–5.
Bai, J., Liu, Y., Yin, X., Duan, H., Ma, J., 2017. Efficient removal of nitrobenzene by Fenton-like process with Co-Fe layered double hydroxide. Appl. Surf. Sci. 416, 45–50.
Basha, S., Keane, D., Morrissey, A., Nolan, K., Oelgemöller, M., Tobin, J., 2010. Studies on the adsorption and kinetics of photodegradation of pharmaceutical compound, indomethacin using novel photocatalytic adsorbents (IPCAs). Ind. Eng. Chem. Res. 49, 11302–11309.
Cao, Z., Yang, S., Wang, M., Huang, X., Li, H., Yi, J., Zhong, J., 2017. Electrodeposition of Cu–Ga precursor layer for $CuGaS_2$ solar energy thin film from alcohol solution. Ionics (Kiel). 23, 1027–1033.
Challagulla, S., Tarafder, K., Ganesan, R., Roy, S., 2017. Structure sensitive photocatalytic reduction of nitroarenes over TiO_2. Sci. Rep. 7, 8783.
Chang, S.-H., Chiu, B.-C., Gao, T.-L., Jheng, S.-L., Tuan, H.-Y., 2014. Selective synthesis of copper gallium sulfide ($CuGaS_2$) nanostructures of different sizes, crystal phases, and morphologies. CrystEngComm 16, 3323–3330.
Chen, C.S., Handoko, A.D., Wan, J.H., Ma, L., Ren, D., Yeo, B.S., 2015. Stable and selective electrochemical reduction of carbon dioxide to ethylene on copper mesocrystals. Catal. Sci. Technol. 5, 161–168.
Chen, P., Qin, M., Chen, H., Yang, C., Wang, Y., Huang, F., 2013. Cr incorporation in $CuGaS_2$ chalcopyrite: a new intermediate-band photovoltaic material with wide-spectrum solar absorption. Phys. Status Solidi Appl. Mater. Sci. 210, 1098–1102.
Cordero, B., Gómez, V., Platero-Prats, A.E., Revés, M., Echeverría, J., Cremades, E., Barragán, F., Alvarez, S., 2008. Covalent radii revisited. Dalton Trans.

2832–2838.
Fujishima, A., Honda, K., 1972. Electrochemical photolysis of water at a semiconductor electrode. Nature 238, 37–38.
Gao, L., Li, Y., Ren, J., Wang, S., Wang, R., Fu, G., Hu, Y., 2017a. Passivation of defect states in anatase TiO_2 hollow spheres with Mg doping: realizing efficient photocatalytic overall water splitting. Appl. Catal. B Environ. 202, 127–133.
Gao, S., Gu, B., Jiao, X., Sun, Y., Zu, X., Yang, F., Zhu, W., Wang, C., Feng, Z., Ye, B., Xie, Y., 2017b. Highly efficient and exceptionally durable CO_2 photoreduction to methanol over freestanding defective single-unit-cell bismuth vanadate layers. J. Am. Chem. Soc. 139, 3438–3445.
Garcia-Segura, S., Brillas, E., 2017. Applied photoelectrocatalysis on the degradation of organic pollutants in wastewaters. J. Photochem. Photobiol. C Photochem. Rev. 31, 1–35.
Gromboni, M.F., Coelho, D., Mascaro, L.H., Pockett, A., Marken, F., 2017. Enhancing activity in a nanostructured $BiVO_4$ photoanode with a coating of microporous Al_2O_3. Appl. Catal. B Environ. 200, 133–140.
Guo, C., Yang, C., Xie, Y., Chen, P., Qin, M., Huang, R., Huang, F., 2016. Preparation of Sn-doped $CuAlS_2$ films with an intermediate band and wide-spectrum solar response. RSC Adv. 6, 40806–40810.
Han, M., Zhang, X., Zeng, Z., 2014. The investigation of transition metal doped $CuGaS_2$ for promising intermediate band materials. RSC Adv. 4, 62380–62386.
Han, M., Zhang, X., Zhang, Y., Zeng, Z., 2016a. The group VA element non-compensated n-p codoping in $CuGaS_2$ for intermediate band materials. Sol. Energy Mater. Sol. Cells 144, 664–670.
Han, M.M., Zhang, X.L., Zeng, Z., 2016b. Sn doping induced intermediate band in $CuGaS_2$. RSC Adv. 6, 110511–110516.
Hashemi, J., Akbari, A., Huotari, S., Hakala, M., 2014. Multi-intermediate-band character of Ti-substituted $CuGaS_2$: implications for photovoltaic applications. Phys. Rev. B - Condens. Matter Mater. Phys. 90, 1–5.
Jensen, S.C., Homan, S.B., Weiss, E.A., 2016. Photocatalytic conversion of nitrobenzene to aniline through sequential proton-coupled one-electron transfers from a cadmium sulfide quantum dot. J. Am. Chem. Soc. 138, 1591–1600.
Jing, W., Wang, Y., Zhu, J., Yao, W., Song, S., 2016. Effects of Ti-doping on $CuGaS_2$ thin films by co-sputtering and sulfurizing. Mater. Lett. 164, 513–515.
Kanakaraju, D., Motti, C.A., Glass, B.D., Oelgemöller, M., 2015. TiO_2 photocatalysis of naproxen: effect of the water matrix, anions and diclofenac on degradation rates. Chemosphere 139, 579–588.
Keum, Y.S., Li, Q.X., 2004. Reduction of nitroaromatic pesticides with zero-valent iron. Chemosphere 54, 255–263.
Khan, A., Rehman, Z. ur, Khan, A., Ambareen, H., Ullah, H., Abbas, S.M., Khan, Y., Khan, R., 2017. Solar-light driven photocatalytic conversion of p-nitrophenol to p-aminophenol on CdS nanosheets and nanorods. Inorg. Chem. Commun. 79, 99–103.
Kim, S.K., Park, J.P., Kim, M.K., Ok, K.M., Shim, I.W., 2008. Preparation of $CuGaS_2$ thin films by two-stage MOCVD method. Sol. Energy Mater. Sol. Cells 92, 1311–1314.
Koskelo, J., Hashemi, J., Huotari, S., Hakala, M., 2016. First-principles analysis of the intermediate band in $CuGa_{1-x}Fe_xS_2$. Phys. Rev. B 93, 165204-1–165204-5.
Kovacic, P., Somanathan, R., 2014. Nitroaromatic compounds: environmental toxicity, carcinogenicity, mutagenicity, therapy and mechanism. J. Appl. Toxicol. 34, 810–824.
Li, T., Liu, S.-S., Qu, R., Liu, H.-L., 2017a. Global concentration additivity and prediction of mixture toxicities, taking nitrobenzene derivatives as an example. Ecotoxicol. Environ. Saf. 144, 475–481.
Li, T., Zhou, Z., He, L., 2017b. A novel approach for enhancing bacterial strains' Nitrobenzene degradation rate. Int. Biodeterior. Biodegrad. 123, 63–69.
Li, X., Jin, X., Zhao, N., Angelidaki, I., Zhang, Y., 2017c. Efficient treatment of aniline containing wastewater in bipolar membrane microbial electrolysis cell-Fenton system. Water Res. 119, 67–72.
Li, Y.P., Cao, H. Bin, Liu, C.M., Zhang, Y., 2007. Electrochemical reduction of nitrobenzene at carbon nanotube electrode. J. Hazard. Mater. 148, 158–163.
Lin, J., Wang, L., 2009. Comparison between linear and non-linear forms of pseudo-first-order and pseudo-second-order adsorption kinetic models for the removal of methylene blue by activated carbon. Front. Environ. Sci. Eng. China 3, 320–324.
Ling, C., Ye, X., Zhang, J., Zhang, J., Zhang, S., 2016. Solvothermal synthesis of CdIn 2 S 4 photocatalyst for selective photosynthesis of organic aromatic compounds under visible light. Sci. Rep. 1–16.
Liu, N., Ding, L., Li, H., Jia, M., Zhang, W., An, N., Yuan, X., 2017a. N-doped nanoporous carbon as efficient catalyst for nitrobenzene reduction in sulfide-containing aqueous solutions. J. Colloid Interface Sci. 490, 677–684.
Liu, X., Su, Y., Lang, J., Chai, Z., Wang, X., 2017b. A novel Au-loaded Na2Ta2O6-multifunctional catalyst: thermocatalytic and photocatalytic elimination of the poisonous nitrobenzene derivatives from wastewater under natural condition. J. Alloy. Comp. 695, 60–69.
Lowenbach, W., Schlesinger, J., King, J., 1979. Toxic Pollutant Identification: Nitrobenzene/Aniline Manufacturing (Washington D.C).
Lv, X., Yang, S., Li, M., Li, H., Yi, J., Wang, M., Niu, G., Zhong, J., 2014. Investigation of a novel intermediate band photovoltaic material with wide spectrum solar absorption based on Ti-substituted $CuGaS_2$. Sol. Energy 103, 480–487.
Ma, L., Wang, J., Wang, H., Zhang, Q., Lu, C., He, X., Li, X., 2017. High halogenated nitrobenzene hydrogenation selectivity over nano Ir particles. Chin. J. Chem. Eng. 25, 306–312.
Marken, F., Kumbhat, S., Sanders, G.H.W., Compton, R.G., 1996. Voltammetry in the presence of ultrasound: surface and solution processes in the sonovoltammetric reduction of nitrobenzene at glassy carbon and gold electrodes. J. Electroanal. Chem. 414, 95–105.
Marsac, R., Pasturel, M., Hanna, K., 2017. Reduction kinetics of nitroaromatic compounds by titanium-substituted magnetite. J. Phys. Chem. C 121, 11399–11406.
Mondal, P., Purkait, M.K., 2017. Green synthesized iron nanoparticle-embedded pH-responsive PVDF-co-HFP membranes: optimization study for NPs preparation and nitrobenzene reduction. Separ. Sci. Technol. 52, 2338–2355.
Palacios, P., Aguilera, I., Wahnon, P., Conesa, J.C., 2008. Thermodynamics of the formation of Ti- and Cr-doped $CuGaS_2$ intermediate-band photovoltaic materials. J. Phys. Chem. C 112, 9525–9529.
Qusti, A.H., Mohamed, R.M., Abdel Salam, M., 2014. Photocatalytic synthesis of aniline from nitrobenzene using Ag-reduced graphene oxide nanocomposite. Ceram. Int. 40, 5539–5546.
Rao, K.V.S., Lavédrine, B., Boule, P., 2003. Influence of metallic species on TiO_2 for the photocatalytic degradation of dyes and dye intermediates. J. Photochem. Photobiol. Chem. 154, 189–193.
Roberts, B.F., Zheng, Y., Cleaveland, J., Lee, S., Lee, E., Ayong, L., Yuan, Y., Chakrabarti, D., 2017. 4-Nitro styrylquinoline is an antimalarial inhibiting multiple stages of Plasmodium falciparum asexual life cycle. Int. J. Parasitol. Drugs Drug Resist. 7, 120–129.
Seshadri, G., Kelber, J.A., 1999. A study of the electrochemical reduction of nitrobenzene at molybdenum electrodes. J. Electrochem. Soc. 146, 3762–3764.
Sheng, T., Qi, Y.J., Lin, X., Hu, P., Sun, S.G., Lin, W.F., 2016. Insights into the mechanism of nitrobenzene reduction to aniline over Pt catalyst and the significance of the adsorption of phenyl group on kinetics. Chem. Eng. J. 293, 337–344.
Song, H., Jiang, H., Liu, T., Liu, X., Meng, G., 2007. Preparation and photocatalytic activity of alkali titanate nano materials $A_2Ti_nO_{2n+1}$ (A = Li, Na and K). Mater. Res. Bull. 42, 334–344.
Song, S., Wang, Y., Yuan, X., Yao, W., Jing, W., 2015. Characterization and preparation of Sn-doped $CuGaS_2$ thin films by paste coating. Mater. Lett. 148, 41–44.
Strandberg, R., Aguilera, I., 2012. Evaluation of vanadium substituted In_2S_3 as a material for intermediate band solar cells. Sol. Energy Mater. Sol. Cells 98, 88–93.
Su, J., Wei, Y., Vayssieres, L., 2017. Stability and performance of sulfide-, nitride-, and phosphide-based electrodes for photocatalytic solar water splitting. J. Phys. Chem. Lett. 8, 5228–5238.
Subbaramaiah, K., Raja, V.S., 1992. Chemical spray deposition of $cugas_2$ thin films. Proc. SPIE 555–558.
Tablero, C., Marron, D.F., 2010. Analysis of the electronic structure of modified $CuGaS_2$ with selected substitutional impurities: prospects for intermediate-band thin-film solar cells based on Cu-containing chalcopyrites. J. Phys. Chem. C 114, 2756–2763.
Tan, C., Nasir, M.Z.M., Ambrosi, A., Pumera, M., 2017. 3D printed electrodes for detection of nitroaromatic explosives and nerve agents. Anal. Chem. 89, 8995–9001.
Ullah, S., Ullah, H., Bouhjar, F., Mollar, M., Marí, B., 2018. Synthesis of in-gap band $CuGaS_2$:Cr absorbers and numerical assessment of their performance in solar cells. Sol. Energy Mater. Sol. Cells 180, 322–327.
Wang, A.J., Cheng, H.Y., Liang, B., Ren, N.Q., Cui, D., Lin, N., Kim, B.H., Rabaey, K., 2011. Efficient reduction of nitrobenzene to aniline with a biocatalyzed cathode. Environ. Sci. Technol. 45, 10186–10193.
Wang, T., Li, X., Li, W., Huang, L., Ma, C., Cheng, Y., Cui, J., Luo, H., Zhong, G., Yang, C., 2016. Transition metals doped $CuAlSe_2$ for promising intermediate band materials. Mater. Res. Express 3, 045905.
Wang, Y., Wang, J., Li, G.X., He, G., Chen, G., 2017. Halogen-bond-promoted photoactivation of perfluoroalkyl iodides: a photochemical protocol for perfluoroalkylation reactions. Org. Lett. 19, 1442–1445.
Wu, Y., Qi, H., Li, B., Zhanhua, H., Li, W., Liu, S., 2017. Novel hydrophobic cotton fibers adsorbent for the removal of nitrobenzene in aqueous solution. Carbohydr. Polym. 155, 294–302.
Xiao, L., Zhu, J., Ding, T., Wang, Y., Fan, Y., Bo, Q., 2015. Synthesis and characterization of Ce-incorporated $CuInS_2$ chalcopyrites. Mater. Lett. 159, 392–394.
Xie, S., Zhang, Q., Liu, G., Wang, Y., 2016. Photocatalytic and photoelectrocatalytic reduction of CO_2 using heterogeneous catalysts with controlled nanostructures. Chem. Commun. 52, 35–59.
Yang, Z., Ma, X., Shan, C., Fang, Z., Pan, B., 2018. Enhanced Nitrobenzene reduction by zero valent iron pretreated with H2O2/HCl. Chemosphere 197, 494–501.
Yang, Z., Xu, X., Liang, X., Lei, C., Gao, L., Hao, R., Lu, D., Lei, Z., 2017. Fabrication of Ce doped UiO-66/graphene nanocomposites with enhanced visible light driven photoactivity for reduction of nitroaromatic compounds. Appl. Surf. Sci. 420, 276–285.
Yuan, Y., Xi, B., He, X., Tan, W., Gao, R., Zhang, H., Yang, C., Zhao, X., Huang, C., Li, D., 2017. Compost-derived humic acids as regulators for reductive degradation of nitrobenzene. J. Hazard. Mater. 339, 378–384.
Zhang, L., He, X., Xu, X., Liu, C., Duan, Y., Hou, L., Zhou, Q., Ma, C., Yang, X., Liu, R., Yang, F., Cui, L., Xu, C., Li, Y., 2017. Highly active TiO_2/g-C_3N_4/G photocatalyst with extended spectral response towards selective reduction of nitrobenzene. Appl. Catal. B Environ. 203, 1–8.
Zhu, L., Ma, B., Zhang, L., Zhang, L., 2007. The study of distribution and fate of nitrobenzene in a water/sediment microcosm. Chemosphere 69, 1579–1585.